

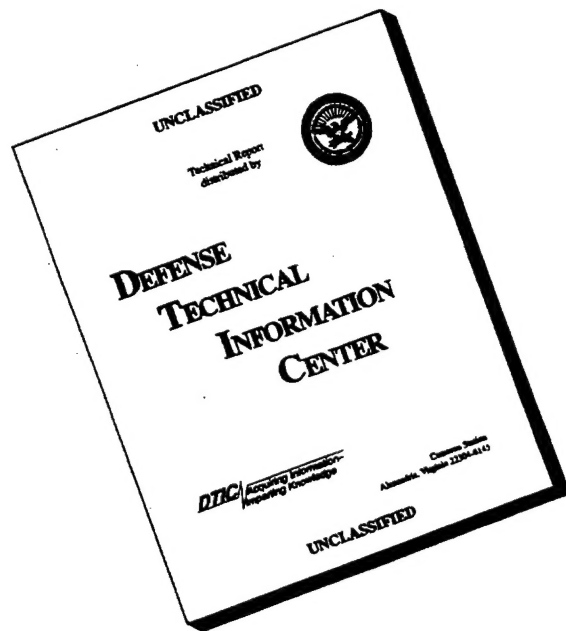
REPORT DOCUMENTATION PAGE

Form Approved
OMB No. 0704-0188

Public reporting burden for this collection of information is estimated to average 1 hour per response, including the time for reviewing instructions, searching existing data sources, gathering and maintaining the data needed, and completing and reviewing the collection of information. Send comments regarding this burden estimate or any other aspect of this collection of information, including suggestions for reducing this burden, to Washington Headquarters Services, Directorate for Information Operations and Reports, 1215 Jefferson Davis Highway, Suite 1204, Arlington, VA 22202-4302, and to the Office of Management and Budget, Paperwork Reduction Project (0704-0188), Washington, DC 20503.

1. AGENCY USE ONLY (Leave blank)		2. REPORT DATE		3. REPORT TYPE AND DATES COVERED Final Technical	
4. TITLE AND SUBTITLE Scanning Tunneling Microscopy and Low Energy Electron Microscopy of Metal Overlayers on Metal Surfaces				5. FUNDING NUMBERS C N00014-89-C-0099	
6. AUTHOR(S) Robert J. Wilson David D. Chambliss					
7. PERFORMING ORGANIZATION NAME(S) AND ADDRESS(ES) IBM Corporation Almaden Research Center 650 Harry Road San Jose, CA 95120-6099				8. PERFORMING ORGANIZATION REPORT NUMBER	
9. SPONSORING/MONITORING AGENCY NAME(S) AND ADDRESS(ES) Office of Naval Research 800 North Quincy Street Arlington, VA 22217-5660				10. SPONSORING/MONITORING AGENCY REPORT NUMBER	
11. SUPPLEMENTARY NOTES <div style="text-align: right; font-size: 2em; font-weight: bold;">19960827 114</div>					
12a. DISTRIBUTION / AVAILABILITY STATEMENT Distribution Statement A - Approved for public release; distribution is unlimited				12b. DISTRIBUTION CODE	
13. ABSTRACT (Maximum 200 words) Thin metal films are of ever increasing importance as the scale of devices shrinks. In order to provide new insight into the atomic details of metal film structure and the nanoscopic details of magnetic domains, efforts were made to study thin metal films on tungsten single crystals using both scanning tunneling microscopy (STM) and spin polarized low energy electron microscopy (SPLEEM). Difficulties were encountered with the as-delivered SPLEEM instrument which required extensive efforts to rectify. STM investigations were directed towards understanding the structure of multilayer metal films on W(111) and Al ₂ O ₃ (0001). Atomic models for a number of different and complex surface structures are derived for Au films on W(110) for coverages between 0.5 and 5 monolayers. STM studies of sputter deposited Pt films on sapphire substrates, for use as seed layers for epitaxial spin valves, are described. By varying the Pt layer thickness and deposition temperature, continuous epitaxial thin films were developed. An epitaxial spin valve was constructed and assessed by magneto-transport measurements. Future opportunities for improved understanding of magnetic and electrical phenomena in thin films are briefly described.					
14. SUBJECT TERMS Scanning Tunneling Microscopy, Low Energy Electron Microscopy, Spin valve, Epitaxi				15. NUMBER OF PAGES 43	
				16. PRICE CODE	
17. SECURITY CLASSIFICATION OF REPORT UNCLASSIFIED	18. SECURITY CLASSIFICATION OF THIS PAGE UNCLASSIFIED	19. SECURITY CLASSIFICATION OF ABSTRACT UNCLASSIFIED	20. LIMITATION OF ABSTRACT UL		

DISCLAIMER NOTICE



THIS DOCUMENT IS BEST QUALITY AVAILABLE. THE COPY FURNISHED TO DTIC CONTAINED A SIGNIFICANT NUMBER OF PAGES WHICH DO NOT REPRODUCE LEGIBLY.

GENERAL INSTRUCTIONS FOR COMPLETING SF 298

The Report Documentation Page (RDP) is used in announcing and cataloging reports. It is important that this information be consistent with the rest of the report, particularly the cover and title page. Instructions for filling in each block of the form follow. It is important to *stay within the lines* to meet *optical scanning requirements*.

Block 1. Agency Use Only (Leave blank).

Block 2. Report Date. Full publication date including day, month, and year, if available (e.g. 1 Jan 88). Must cite at least the year.

Block 3. Type of Report and Dates Covered. State whether report is interim, final, etc. If applicable, enter inclusive report dates (e.g. 10 Jun 87 - 30 Jun 88).

Block 4. Title and Subtitle. A title is taken from the part of the report that provides the most meaningful and complete information. When a report is prepared in more than one volume, repeat the primary title, add volume number, and include subtitle for the specific volume. On classified documents enter the title classification in parentheses.

Block 5. Funding Numbers. To include contract and grant numbers; may include program element number(s), project number(s), task number(s), and work unit number(s). Use the following labels:

C - Contract	PR - Project
G - Grant	TA - Task
PE - Program Element	WU - Work Unit Accession No.

Block 6. Author(s). Name(s) of person(s) responsible for writing the report, performing the research, or credited with the content of the report. If editor or compiler, this should follow the name(s).

Block 7. Performing Organization Name(s) and Address(es). Self-explanatory.

Block 8. Performing Organization Report Number. Enter the unique alphanumeric report number(s) assigned by the organization performing the report.

Block 9. Sponsoring/Monitoring Agency Name(s) and Address(es). Self-explanatory.

Block 10. Sponsoring/Monitoring Agency Report Number. (If known)

Block 11. Supplementary Notes. Enter information not included elsewhere such as: Prepared in cooperation with...; Trans. of...; To be published in.... When a report is revised, include a statement whether the new report supersedes or supplements the older report.

Block 12a. Distribution/Availability Statement.

Denotes public availability or limitations. Cite any availability to the public. Enter additional limitations or special markings in all capitals (e.g. NOFORN, REL, ITAR).

DOD - See DoDD 5230.24, "Distribution Statements on Technical Documents."

DOE - See authorities.

NASA - See Handbook NHB 2200.2.

NTIS - Leave blank.

Block 12b. Distribution Code.

DOD - Leave blank.

DOE - Enter DOE distribution categories from the Standard Distribution for Unclassified Scientific and Technical Reports.

NASA - Leave blank.

NTIS - Leave blank.

Block 13. Abstract. Include a brief (Maximum 200 words) factual summary of the most significant information contained in the report.

Block 14. Subject Terms. Keywords or phrases identifying major subjects in the report.

Block 15. Number of Pages. Enter the total number of pages.

Block 16. Price Code. Enter appropriate price code (NTIS only).

Blocks 17. - 19. Security Classifications. Self-explanatory. Enter U.S. Security Classification in accordance with U.S. Security Regulations (i.e., UNCLASSIFIED). If form contains classified information, stamp classification on the top and bottom of the page.

Block 20. Limitation of Abstract. This block must be completed to assign a limitation to the abstract. Enter either UL (unlimited) or SAR (same as report). An entry in this block is necessary if the abstract is to be limited. If blank, the abstract is assumed to be unlimited.

**Scanning Tunneling Microscopy and Low Energy Electron Microscopy
of Metal Overlayers on Metal Surfaces.**

Final Report

Contract No. N00014-89-C-0099

R. J. Wilson and D. D. Chambliss

IBM Research Division

Almaden Research Center

San Jose, CA 95120

Thin metal films are of ever increasing importance as the scale of devices shrinks. In order to provide new insight into the atomic details of metal film structure and the nanoscopic details of magnetic domains, efforts were made to study thin metal films on tungsten single crystals using both scanning tunneling microscopy (STM) and spin polarized low energy electron microscopy (SPLEEM). Difficulties were encountered with the as-delivered SPLEEM instrument which required extensive efforts to rectify. STM investigations were directed towards understanding the structure of multilayer metal films on W(111) and $\text{Al}_2\text{O}_3(0001)$. Atomic models for a number of different and complex surface structures are derived for Au films on W(110) for coverages between 0.5 and 5 monolayers. STM studies of sputter deposited Pt films on sapphire substrates, for use as seed layers for epitaxial spin valves, are described. By varying the Pt layer thickness and deposition temperature, continuous epitaxial thin films were developed. An epitaxial spin valve was constructed and assessed by magneto-transport measurements. Future opportunities for improved understanding of magnetic and electrical phenomena in thin films are briefly described.

Introduction

Thin metal films are becoming increasingly important as magneto-resistive sensors progress. Present day devices employ multiple layers of magnetic and electrically conducting materials, some of which are only 2 or 3 atoms thick.^{1,2} Metal film growth and structure then become of extreme importance as crystalline texture, connectivity, and magnetic domain structure are critical issues for device performance which remain poorly understood. In efforts to approach these problems from a fundamental perspective, scanning tunneling microscopy and spin polarized low energy electron microscopy have been used to study thin metal films at the limits of spatial resolution presently available. As technical problems with the as-received LEEM instrument caused delays in collaborative investigations, efforts made with these two techniques are described separately.

Scanning Tunneling Microscopy of Metal Films

The initial phase of this work involved the analysis of data relating to the surface structure of thin films of Au on the W(111) surface. Detailed atomic models have now been constructed which give the first accounting for the myriad of surface structures which arise as Au is deposited by thermal evaporation in films which ranged from 0.5 to 7 monolayers (ml) in thickness. The surprising variety of surface structures can all be accounted for with relatively simple models for the Au layers. At coverages below 1 ml the Au layers appear initially as weakly incommensurate islands which transform at layer completion into a compact pseudomorphic layer with two domains associated with Au occupancy of two fcc sites on the bcc W(110) surface. At 2 ml a highly corrugated surface develops, complete with vacancies at each corner of the surface unit cell, indicating the transition of the Au layer to a nearly hexagonal geometry consistent with preferred fcc(111) packing of dense Au layers. For 3 ml and higher coverages the STM images are readily interpreted in terms of hexagonal layers which gradually change in lattice constant towards the bulk Au values. A gradual transformation in the STM images for even thicker layers is explained as a Moire interference pattern between the nearly hexagonal underlying layers and a surface layer which continuously transforms into the the uniaxial "23" Au(111) surface reconstruction. A preprint of this paper which describes these surface structures and a surprising island growth phenomena, not discussed here, is enclosed.

The extension of STM work to thick films has also included the study of films formed by sputtering techniques and to the use of insulating crystal substrates which allow characterization of magneto-electrical transport phenomena. Metal films can presently be produced in two new sputtering

systems which are attached to chambers for in situ characterization by STM, XPS, and LEED. Ex situ analysis of thin film magnetoresistance using a four point probe and 250Oe Helmholtz coils and of magnetic characteristics by vibrating sample magnetometry are also available. Sputtering facilities include a triple 2" magnetron cluster which utilizes Ar at 200V and 5mTorr and a 6 target ion beam system which uses Ar, Kr, or Xe ions near 1000V and 0.2Torr. Base pressures are low, 10^{-9} Torr, and deposition rates are near 1Å/sec. for both systems. These systems have been used previously to study significant differences between films produced by the two sputtering techniques which differ primarily in the energy distributions of the deposited atoms and result in different film structure and magnetics.^{3,4}

Efforts at studying the growth of thin magnetic films on insulating substrates were begun with STM, LEED, and XPS characterizations of the growth of Pt(111) films on Al_2O_3 . This system was chosen for chemical and thermal robustness and because the molecular beam epitaxy growth of platinum films at elevated temperatures is known to produce "seed layers" which allow for room temperature epitaxial growth of FCC films of copper and cobalt.⁵ These two metals are of great interest for Giant Magneto-Resistance multilayer structures and for spin valve related devices. The insulating character of the substrate poses a possible limitation for STM and it is unclear what minimum metallization thickness is required for reliable operation. To provide clear and interpretable data we prepared the sapphire substrates by annealing 1cm² squares at 1400°C for 24 hours in air. This recipe has produced wafer samples in air which are nearly atomically flat.^{6,7} These coupons were loaded into ultra high vacuum, heated, sputtered with Ar, and annealed to 1000°C to produce substrates which were free from contamination and which produced 1x1 LEED patterns indicative of an ordered surface. The clean substrates were then heated to near 600°C and coated with varying thicknesses (5-50Å) of Pt using an ion beam Xe⁺ source operating at 850V. Deposition rates are typically 0.5Å/sec.

To evaluate the initial substrate smoothness, the sputter cleaning step was eliminated and the deposition of a thin (5Å) Pt film was performed at room temperature. STM images were obtained very easily on these very thin films as shown in Figure 1(a,b.) The wide scan image, (a), shows a fairly rough Pt film decorating a presumably flat substrate which is punctuated by 3 monoatomic substrate steps spaced about 500Å apart. The Pt grains appear to be about 20Å in diameter and the variations in grain height can be associated with discrete numbers of Pt layers within each grain. Unfortunately, XPS revealed the presence of substantial Ca impurities on the heated substrates and a sputter etch was required to remove these impurities and their possible effects in preventing epitaxy of the films grown at high temperatures. The sputter cleaning procedure was a 5 minute exposure to a 5µa/cm², 1000V Ar⁺ beam, followed by

a 5 minute anneal to 1000°C. When 5Å of Pt were deposited on such substrates at room temperature, the STM images, Figure 2, revealed a long period (100Å) irregular surface corrugation several Å in height which must be associated with the sputter-annealing procedure as the Pt grain structure appears otherwise unaffected. Neither of these low temperature deposited Pt films produced LEED patterns, although STM data suggests that the individual grains are likely (111) oriented crystallites.

Once the basic morphology, cleanliness, and order of the substrate were reliably established, studies of Pt films deposited at near 600°C were begun. Figure 2(a) shows a 2000Å wide image of a 10Å thick Pt film. Here and in the 600Å wide image in Fig. 2(b), one sees 100Å diameter isolated grains with distinctive heights. Monoatomic Pt steps can be seen in the grain near the lower right corner of Figure 2(b). The gaps between crystallites are quite deep and likely extend completely to the substrate. Figure 2(c,d,e) show 2000, 600, and 200Å wide images for a 15Å Pt film. The grains appear slightly smaller and somewhat more dense as expected for the onset of film coalescence. Fig. 2(e) demonstrates the frequent appearance of hexagonal, crystallographic structures in monosteps atop a grain. Figure 3(a,b) show 2000Å and 600Å wide images for a 30Å thick Pt film grown at 580°C. This film is nearly completely coalesced in that separate grains can no longer be identified and that, except for a few small islands, the net substrate slope can be detected from the density of continuous Pt steps at the surface. There are, however, numerous pinholes which are likely associated with gaps between underlying crystallites which have not filled in. Preferred crystallographic directions are evident at many of the step edges. Fig. 3(c) shows a 2000Å wide image of a 50Å thick Pt film grown at 600°C. At this thickness and temperature there are few pinholes but the overall flatness is considerably reduced compared to Fig. 3(a). The extended terrace structure seen in Fig. 3(a) was not frequently observed and we believe this particular sample was grown at an optimum temperature falling in a very narrow temperature range near 580°C. At growth temperatures below 500°C, as for the room temperature, no surface order was found using LEED but even thin films tend to more continuous. At temperatures above 600°C, the lateral grain size is larger but the surface is rougher and there is a tendency toward grain separation and pinholes. This variable morphology is presumably due to a competition between thermally activated diffusion of Pt on Pt, which helps surface order and smoothness, and the thermodynamic tendency for Pt to de-wet the low surface energy Al_2O_3 substrate. The results shown here demonstrate a very narrow temperature window for simultaneously optimizing crystalline order, crystallite coalescence and surface flatness. To improve this situation we have tried post-annealing 20Å films deposited at room temperature at 600°C but surface order did not obtain. We have also attempted to anneal 20Å films deposited at near 600°C at annealing temperatures near 900°C. These films produced LEED patterns which showed charging effects indicative

of bare regions of Al_2O_3 , indicative of substantial de-wetting and islanding of the Pt film. STM images were consistent with this hypothesis in that tall mounds were observed. Furthermore STM bias voltage thresholds were observed, suggesting either conductivity limitations or the involvement of surface states of the bare insulating Al_2O_3 substrate. Too little data was taken to allow unambiguous interpretation of the STM images which are therefore not shown. One application of these films is in studies of advanced GMR sensors where the implications of surface roughness for interlayer magnetic coupling, magnetoresistance amplitudes, and antiferromagnetic exchange bias coupling strengths remain poorly understood. In an effort to test whether such issues can be addressed using the Pt seed layers described above we have used a 30Å Pt layer to grow an ion beam sputtered epitaxial spin valve structure of the form 30Pt/30Co/30Cu/30Co/150MnFe/50Ta. This device² gave $\delta R/R = 5\%$ with a free layer coercivity of 100e, a 100e ferromagnetic coupling field and a 1500e exchange coupling of the pinned layer.

Further STM work on the magnetic and spacer layers of such epitaxial devices will provide insight into the role of surface roughness in antiferromagnetic and ferromagnetic coupling in multilayer and spin valve structures. Alternatively, the grain and pinhole structure encountered for Pt films at excessive temperature or inadequate thicknesses is of interest for films of thin, highly coercive materials used in magnetic storage media where small ferromagnetic grains which are physically separated are required in order to achieve high densities.

IBM research using LEEM

Introduction

IBM's spin-polarized low-energy electron microscope (SP-LEEM) is a unique instrument for studying surface magnetism and surface structure simultaneously, in the same samples. The research under this contract has aimed at measuring magnetic domain structures in ultrathin films grown *in situ*. Operational difficulties with the instrument in its as-delivered state, however, which arose after the proposal for this grant was submitted, showed that SP-LEEM is a more difficult technique than was expected. IBM's accomplishments thus far pertain to the techniques and requirements of SP-LEEM, and not to the science that will later be achieved.

Research accomplishments

One important accomplishment was discovering the need for thorough protection against discharges when a high-voltage instrument in vacuum incorporates Inchworm motors, and finding a way to provide that protection. The SP-LEEM presents unusual requirements because electrostatic lenses are used throughout, in order to preserve spin polarization in the electron beam. When operating according to its optical design, many elements are held at +5kV with respect to ground. Because the entire optical assembly is operated within a baked UHV chamber, maintaining this high-voltage isolation presents no serious problems in a quiescent state. However, in the original configuration, any movement of the two apertures in the optical column--movement that is essential for SP-LEEM operation--would trigger high-voltage discharges sufficient to disable critical electronic components. It was found that the piezoelectric "Inchworm" motors (from Burleigh Instruments) generated frictional gas bursts and very small plasma discharges between the motor electrodes. These discharges were in turn enough to trigger the large damaging discharges in the SP-LEEM. A major task was to design, install, and test a solution to this, in which smaller Inchworm motors were used and surrounded with polyimide shells to keep the discharges away from the highest-field regions. Before this was accomplished the microscope could only be operated well below its design point (1.5kV instead of 5kV) with, consequently, severely degraded performance. The modification has now been made and operation to 5kV has been tested successfully.

A second accomplishment was establishing the operating parameters of the full-sphere spin-polarized electron source. Protocols have been established for preparing the photocathode, for producing, measuring, and optimizing beam current, and for providing a viable lifetime for the spin-polarized electron beam. Most important, SP-LEEM operation was demonstrated on a film of Co on W(110) (using the degraded 1.5kV parameters discussed above) in which domains of opposite in-plane magnetizations were observed in an 8- μ m field of view. The experiments showed in particular that varying the polar and azimuthal angles of the polarization direction yielded exactly the extinction and reversal of contrast expected for the sample's in-plane magnetization. Thus it was demonstrated for the first time that this spin-polarized electron gun performs according to design, and the microscope optics indeed preserves spin polarization according to its design.

The third major accomplishment has been to determine what capabilities must be incorporated into the sample manipulator and sample cartridge if successful research is to be conducted with an SP-LEEM. The tilt motions of the sample, which are indispensable for aligning the instrument, must be stable and *completely reliable*, as must be the sample translations. Sample preparation in the microscopy position must also be possible, including sample cleaning and heating and film deposition. The original manipulator was designed to incorporate all these functions, but did so without sufficient protection to

ensure reliability. At several times during the span of this contract, all other elements were in place to conduct research with the SP-LEEM, yet failures in the manipulator required disassembly of the instrument. Many repairs and small modifications were tried to work around the flawed design but these were ultimately unsuccessful. When the scope of the problem became clear, IBM undertook to replace the manipulator with one having a simpler, tested, mechanical design. This change to IBM's capital equipment of course falls outside the scope of the present contract, but it will foster the successful scientific research originally planned in this program.

A fourth accomplishment that will be of considerable scientific value is the determination of appropriate parameters for sample-magnetization coils to be incorporated into the SP-LEEM in the microscopy position. An important scientific goal not anticipated in the original SP-LEEM design is to measure *in situ* the response of magnetic domains in thin films to applied magnetic fields. The instrument is designed to exclude all stray fields, since any distortion in the trajectories of the low-energy imaging electrons impinging on the sample will degrade imaging performance. Thus samples are to be studied in remanence, i.e. with no applied field. However, changes in the remanent state can be induced by pulsed fields, and these will not interfere with SP-LEEM operation provided there are no stray fields from ferromagnetic parts in the vicinity of the sample. The ferromagnetic films to be studied in this project will normally be formed by deposition in a macroscopically unmagnetized state, and these could be modified *in situ* in two complementary ways. A strong applied field can yield nearly complete magnetization, at least in the region visible to the SP-LEEM which is far from the demagnetizing effects of edges. In such a state, and in stages of magnetization reversal from that state, the role of structural defects in the film as nucleation or pinning sites for magnetic domain changes can be observed directly. It is unlikely that the magnetic fields from the sample itself will interfere with imaging because the magnetized volume is so small. The complementary approach is to examine a macroscopically demagnetized sample whose microscopic state is repeatedly changed by alternating pulses of an appropriate magnetic field. The inherent speed of SP-LEEM should permit the acquisition of a useful ensemble of distinct states so that a statistical analysis of domain reversals is possible.

Our concrete progress in this direction has been to design, build, install, and characterize fully a set of prototype coils for this purpose. The design constraints may seem prohibitive: the coil windings can occupy only a few cm³; the coils cannot be close to the sample because the sample must sometimes be heated above 2000K; no pole pieces may be used to focus flux because of their remanent magnetization; and water cooling of the coils is impractical because of space constraints and possible vibration problems. Despite this, however, it was found that pulse fields of several hundred Oe could routinely be applied

by controlled capacitor discharge. The limitation is the heating of the windings, which is monitored using the winding resistance. When the new manipulator is installed, the prototype coils will be discarded, and new coils designed with more winding volume, better thermal shielding and heat sinking, and optimized impedance match to the pulse supply will be produced.

Some lesser accomplishments are worth noting as part of the necessary progress toward conducting significant research with the SP-LEEM. Ultra high vacuum is essential for the planned surface-magnetism research, so it has been essential to develop procedures for proper chamber bakeout, as well as sample cleaning, characterization using Auger spectroscopy, and controlled deposition from evaporative metal sources. In addition to the usual UHV requirements, the deposition facility required that the positioning of the SP-LEEM in its chamber be measured accurately and modified so that deposition will be centered on the sample surface. In the course of this work we have established recipes for cleaning W crystals and Si(111) surfaces in our vacuum system.

Planned future research

Although the term of the contract is finished the scientific work will continue. The first thorough work will be on relatively well-understood ferromagnetic metals on W(110). As has been described above, a focus of subsequent work will be the magnetic response of magnetic films to field pulses. Other possibilities for measuring dynamic magnetic properties of thin films and surfaces are also being examined. One side benefit of the new manipulator is that it will facilitate the addition of new capabilities like sample cooling and auxiliary electrical contacts to the sample, which could not be accommodated in the original equipment.

In order to produce the most scientific value from the unique SP-LEEM instrument, IBM has elected to donate it to Lawrence Berkeley Laboratories, for eventual use as a facility accessible to the general science community. Development of new capabilities and extension of scientific applications will continue in a collaboration between IBM and LBL personnel. It is expected that the instrument will be relocated to the Berkeley site by the end of 1996. This separation eliminates inter-grain exchange coupling so that each grain can respond separately, except for weak magnetostatic coupling, to magnetic field used to write magnetic bits. In this case the physical separation of the grains of the thin Pt films grown near 600°C is of great value. It is likely that similar phenomena operate for high coercivity, high remanance, and high temperature alloys currently being explored for storage media applications in the same film thickness regime as has been examined here.

References

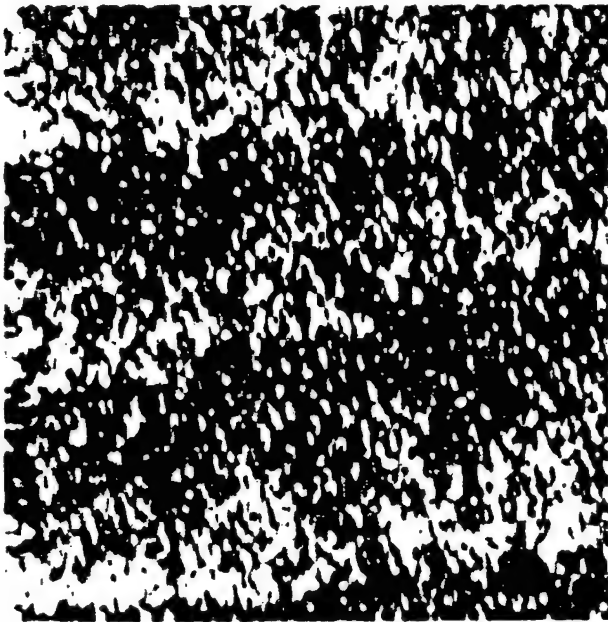
1. S. S. Parkin, R. F. Farrow, R. F. Marks, A. Cebollada, G. R. Harp, and R. J. Savoy, **Phys. Rev. Lett.** 72, 3718 (1994).
2. D. E. Heim, R. E. Fontana, Jr., C. Tsang, V. S. Speriosu, B. A. Gurney and M. L. Williams, **IEEE Trans. Mag.** 30 316 (1994).
3. T. J. Minvielle, R. L. White and R. J. Wilson, **J. Appl. Phys.** 79, 5116 (1996).
4. T. J. Minvielle, R. J. Wilson and R. L. White, **Appl. Phys. Lett.** 68, 2750 (1996).
5. R. F. C. Farrow, G. R. Harp, R. F. Marks, T. A. Rabadeau, M. F. Toney and D. Weller, **J. Cryst. Growth** 133, 47 (1993).
6. M. Yoshimoto et al, **Appl. Phys. Lett.** 67, 2615 (1995).
7. Y. Kin and T. Hsu, **Surf. Sci.** 258, 131 (1991).

Figure Captions

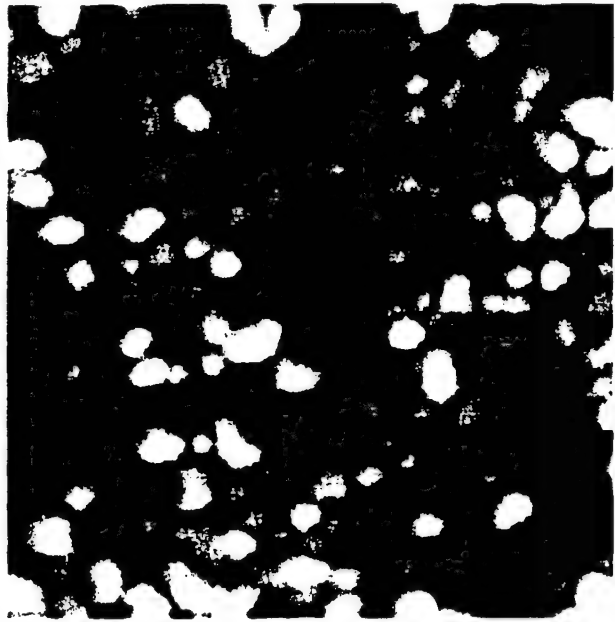
Fig. 1 STM images of 5 Å Pt films deposited at room temperature. (a) (2000 Å x 2000 Å) and (b) (600 Å x 600 Å) images for unspattered Al₂O₃ substrate. (c) (2000 Å x 2000 Å) and (d) (600 Å x 600 Å) images for sputtered substrate.

Fig. 2 STM images of Pt films deposited at 580-590°C. 10 Å film: (a) (2000 Å x 2000 Å) and (b) (600 Å x 600 Å). 15 Å film: (c) (2000 Å x 2000 Å), (d) (600 Å x 600 Å), (e) (200 Å x 200 Å). 30 Å film:

Fig. 3 STM images of Pt films deposited at 580-590°C. 30 Å film: (a) (2000 Å x 2000 Å) and (b) (600 Å x 600 Å) 50 Å film: (h) (2000 Å x 2000 Å).



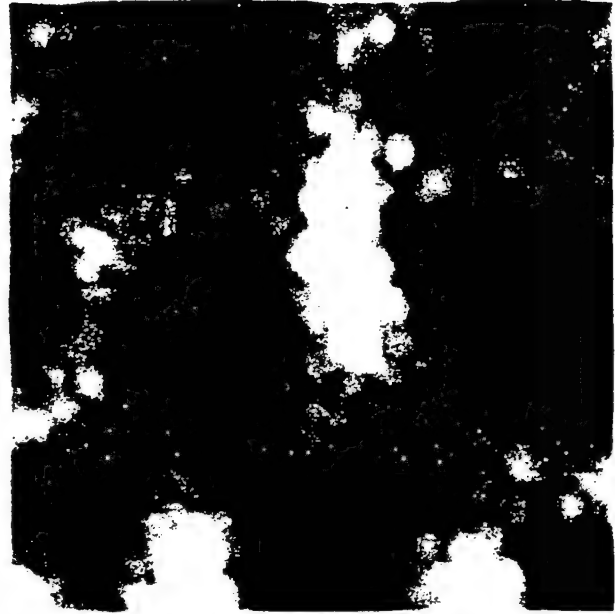
a



b

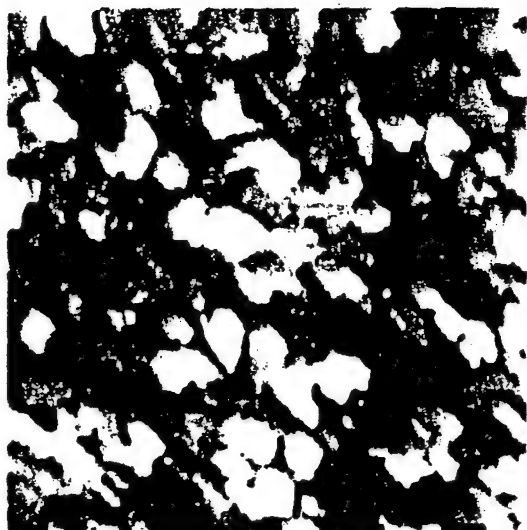


c

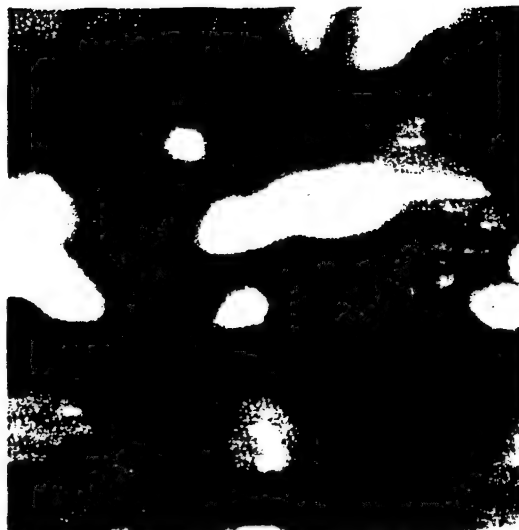


d

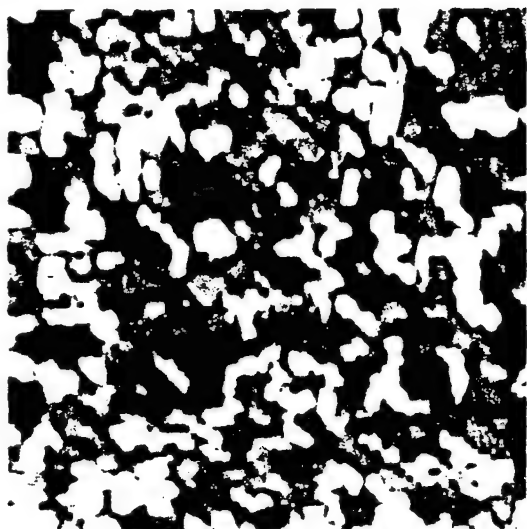
Fig. 1



a



b



c



d



e

FIG 2



a



b



c

An STM Study of Epitaxially Grown Pt Films Sputter Deposited on Basal-plane Sapphire

M. L. Hildner, T. J. Minvielle, and R. J. Wilson

IBM Research Division, Almaden Research Center, 650 Harry Road, San Jose CA
95120-6099

Abstract

Epitaxial Pt films of various thicknesses were grown on basal-plane sapphire using ion beam sputtering. STM images are used to characterize the film morphologies and their dependence on deposition temperature, T_D . Epitaxial quality is determined by low-energy electron diffraction (LEED). The film morphologies are very sensitive to T_D — exceeding the narrow ideal temperature range of 580-590°C means the difference between a relatively flat Pt film and a surface with tall Pt mounds separated by bare sapphire patches. Within this temperature range, Pt islands are observed at 10 Å, these islands begin to coalesce at 15 Å, and continuous films are observed at 30 Å and 50 Å. The continuous films are far from ideal atomically flat surfaces: both show several exposed Pt layers and the 30 Å film has many pin holes. Also, images of 5 Å Pt films deposited at room temperature are used to characterize the substrate morphology.

The growth of epitaxial metal films on metal-oxide surfaces is of interest for both applied and fundamental reasons. These films should prove useful as substrates for devices with magnetoresistive, ferroelectric, magneto-optic, and other applications. Epitaxial films also currently provide the opportunity to study film and multilayer properties that are dependent on crystalline growth direction. Since it is expected that device quality will be improved and epitaxial growth enhanced with the fabrication of atomically flat substrates and sharp interfaces, a real space structural characterization approaching the atomic scale is necessary for a complete understanding of how growth conditions affect film morphology. For this reason we investigate here the growth of ultrathin Pt films on basal-plane sapphire with a scanning tunneling microscope (STM).

The motivation for selecting this system arises from the considerable attention recently directed at the role of epitaxy on the novel properties of artificial magnetic multilayers [1,2]. Significant among these properties is giant magnetoresistance (GMR) due to its potential for device applications [3,4]. Insulating substrates are useful for application and investigation of GMR as they avoid the current shunting of metal substrates and minimize the chemical reactions between the film and substrate that often occur for semiconducting substrates. It is, however, frequently necessary to grow an epitaxial metallic seed film to initiate the desired growth characteristics for the multilayer films and the thickness of this seed film must be restricted to less than 100 Å to minimize current shunting. For the basal-plane sapphire or $\text{Al}_2\text{O}_3(0001)$ surface, it has previously been shown that under suitable growth conditions, Pt, when deposited by molecular beam epitaxy (MBE), can provide a near ideal ultrathin seed film for a wide variety of MBE grown GMR structures [2,5]. However, GMR and other thin film and multilayer devices are frequently fabricated with growth techniques other than MBE. In this study, we demonstrate that Pt seed films of comparable epitaxial quality can be obtained with sputter deposition [6].

There has also been some effort to improve preparation techniques of sapphire substrates as, even when highly polished, these surfaces have irregular corrugations and high defect densities. An in-air annealing procedure and its affect on surface morphology has recently been studied with atomic force microscopy (AFM) [7]. Atomically smooth surfaces with wide terraces ($\sim 3000\text{\AA}$) and straight atomic steps were obtained by annealing polished sapphire samples in air at temperatures between 1000 and 1400°C. Minimum height steps were found at the lower temperature anneals while step bunching occurred at higher temperature. However, the cleanliness or purity and thus the applicability of samples prepared in this manner remains to be determined. An earlier reflection electron microscopy (REM) study of sapphire samples annealed in air at

1400°C for 24 hours also revealed large terraces [8] but, while conducted in UHV, surface cleanliness was not characterized in this study.

Reflection high-energy electron diffraction (RHEED), low-energy electron diffraction (LEED), and X-ray photoelectron spectroscopy and diffraction (XPS, XPD) were used in the previously mentioned study of MBE grown Pt seed films [5]. The samples in this study — which were prepared by polishing and chemically etching the surface outside the MBE system and annealing at 600°C for 20 minutes in UHV — had residual C and, occasionally, Si and F impurities. The optimal substrate temperature for growth, T_s , was determined to be 600°C. With this condition, the Pt nucleated as rotationally twinned islands with an epitaxial relationship of $\text{Pt}[111] \parallel \text{Al}_2\text{O}_3[0001]$ and $\text{Pt}(110) \parallel \text{Al}_2\text{O}_3(10\bar{1}0)$. The measurements suggested that at 15 Å the Pt film is nearly continuous and island coalescence occurs between 15 and 30 Å. In contrast, 30 Å thick films for $T_s > 650^\circ\text{C}$ were not continuous and films for $T_s < 550^\circ\text{C}$ lacked some in-plane coherence.

Our STM topographs combined with LEED show similar results for sputter deposited films; but more importantly they reveal additional information regarding the surface morphology unobtainable with the diffraction methods used in the study above. Our results confirm the epitaxial relationships and reveal film continuities consistent with those of the diffraction study. Beyond these findings, however, we have been able to characterize (with the STM topographs) substrate morphology and — as a function of film thickness and deposition temperature — film flatness, island sizes, and defects.

The experiments were carried out in a previously described UHV system (base pressure 1×10^{-10} Torr) consisting of the following [9]: a preparation chamber equipped with an electron bombardment heating stage, an Ar sputter source, LEED, and XPS; an STM chamber; and an interconnecting transfer chamber. This system now includes an attached sputter deposition chamber. The sapphire substrates were made by dicing into 8 mm x 10 mm pieces a 2 inch diameter disk (call Union Carbide about cut tolerance and polishing). To ensure an ultra-flat surface, the samples were annealed at 1400°C in air for 24 hours [8]. The samples were then fastened with Ta wire clips onto a rectangular Ta plate having dimensions comparable to the sample and spot-welded onto a Ta plug. The Ta clips wrapped around to the front of the sample and, following Pt deposition, provided electrical contact for films as thin as 5 Å. Upon insertion into the preparation chamber, C and Ca impurities were seen in XPS spectra and, although sample charging occurred for incident beam energies ≤ 100 eV, a weak (1x1) LEED pattern could be seen at higher energies. After annealing to 1000°C for 12 minutes, all C was removed and a fair 3-fold symmetric (1x1) diffraction pattern, characteristic of the bulk hexagonal

symmetry, was exhibited in LEED down to 35 eV before charging. An e-beam filament positioned behind the sample and a pyrometer aimed at the front were used for heating and temperature measurement, respectively. Care was taken to avoid annealing temperatures exceeding 1000°C as these would lead to reconstructions of the $\text{Al}_2\text{O}_3(0001)$ surface [10,11]. Removal of the Ca required an Ar sputtering step (1 keV, 20 mA) prior to the UHV anneal. The STM topographs will show that this left some residual surface roughness that could not be annealed out at 1000°C.

After cleaning, the samples were transferred to the sputter chamber for Pt deposition. The Ta sample holder plug was inserted into a block which was resistively heated for elevated temperature depositions. There was no line of sight to the sample for the pyrometer, so the temperatures reported here are of the back of the Ta plate. The deposition system is comprised of an ion beam source where 850V Ar^+ ions are directed at a Pt target leading to Pt deposition rates of 1 Å/sec. A new sample was used for each deposition as it was not clear that an old one could be restored: evaporation of deposited Pt was not possible as heating to 1450°C, the maximum temperature of our heating stage, lead to the formation of very thick (probably on the order of a few 100 Å) Pt crystallites on a predominantly bare surface; and extensive sputtering left traces of Pt.

We have characterized the sapphire substrate morphology by depositing, at room temperature, 5 Å of Pt on samples for which cleaning did and did not include the sputtering step. Fig. 1 shows typical STM topographs of these surfaces which showed no diffraction spots in LEED. The large area image for the unsputtered substrate [Fig. 1(a)] is very rough but shows large terraces that are 1000 Å or more wide. Fig. 1(b), a higher magnification image of the same surface, shows that the Pt atom surface mobility at room temperature is sufficiently small to create many nuclei of small size which results in a nearly continuous film. Seven exposed layers are seen in this image and the islands are all flat topped (this latter observation implies that the islands are epitaxial and that the lack of diffraction spots in LEED is due to incoherent scattering between the small ~30 Å wide islands — apparently diffraction techniques are not always superior to imaging techniques in establishing epitaxy). The image of Fig. 1(b) also exhibits a coverage distribution for the exposed layers that is Poisson-like. As a Poisson distribution is indicative of ideal three-dimensional growth in which all adatoms are confined to the layer on which they land, it appears that all the roughness is due to the Pt atoms — which have a low diffusivity — and that the substrate is atomically flat. Thus we concur with the REM and AFM studies that the in-air annealing process produces an atomically flat surface with wide terraces. However, this surface is not free of impurities. When Ar sputtering is used for complete substrate cleaning, the wide terrace structure is eliminated

by a long length scale corrugation of the surface as seen in Fig. 1(c) and 1(d). This structure is characteristic of the substrates used for all the Pt films deposited and examined in this work.

Pt films of various thicknesses were grown with the substrate at a number of elevated temperatures. The quality (*i.e.*, flatness and continuity) of these films was very sensitive to the deposition temperature with the best films produced in the narrow temperature range of 580-590°C. A 20 Å film grown at 500°C had a poor LEED pattern and showed a high nucleation density in STM. Good quality LEED patterns were observed for films grown above 590°C (ranging from 5-30 Å thick) but these showed charging at low energies indicative of bare substrate. Exposed substrate regions in these films were confirmed by the STM images which also showed very tall mounds of Pt (these STM images are not included here as they are difficult to interpret due to the large variations in height and bare insulating substrate).

Films of 10 Å, 15 Å, 30 Å, and 50 Å were grown in the optimal range of 580-590°C. Typical STM topographs for these films are shown in Fig. 2. The corresponding LEED patterns in each case showed no evidence of sample charging and looked much like the pattern for the bare surface except that they had a 6-fold symmetry indicative of rotational twinning. This twinning has previously been interpreted as arising from the creation of two kinds of 3-fold terraces in the presence of steps on the sapphire substrate [5,12]. With a corundum structure (hexagonal unit cell with $a=4.76$ Å and $c=13.00$ Å) a perfect (0001) sapphire surface has 3-fold symmetry and allows only one orientation for a Pt(111) film which also has 3-fold symmetry. However, on a stepped surface with step heights equal to an odd multiple of the minimum step height ($c/6$), two different Pt(111) orientations are allowed since two kinds of terraces are formed with nucleation sites that differ in symmetry by a 60° rotation. With this interpretation, the epitaxial relationship of $\text{Pt}[111] \parallel \text{Al}_2\text{O}_3[0001]$ and $\text{Pt}(110) \parallel \text{Al}_2\text{O}_3(10\bar{1}0)$ is deduced from the LEED pattern.

The topographs in Fig. 2(a) and (b) are for a 10 Å Pt film deposited at a substrate temperature of 590°C. At this coverage the film is comprised of separate islands that range in width by ~40-300 Å. The islands have varying heights (~7-8 exposed layers) and, between them, there are deep spaces that probably extend down to the substrate. The large area image includes a substrate step that is several times the minimum step height and was therefore not obscured by the multilayered Pt film. There must be few of these large substrate steps formed in the cleaning process as this was the only one observed in the many (~100) sample areas examined. More significantly, a comparison of the topographs of Figs. 1(d) and 2(b) show that the Pt island height variations appear uncorrelated with the corrugation of the sputtered substrate.

Commencement of island coalescence is seen in the topographs in Figs. 2(c)-(e) for a 15 Å Pt film deposited at a substrate temperature of 580°C. There are still several exposed layers and, although there are still deep troughs between many of the now larger "islands", there is an overall connectedness to the film. Also, several Pt steps are now frequently seen on top of the film at this thickness [Fig. 2(e)]. These steps show hexagonal faceting — a possible equilibrium shape which suggests that diffusion along step edges is not kinetically limited.

A continuous film is formed at 30 Å (580°C deposition temperature) as seen in the topographs of Fig. 3(a) and (b). There are still many exposed layers (~7) and a high density of deep pin holes. On the other hand, the film is much smoother than the bare (sputtered) surface. There are also other defects that appear as small (~2-20 Å) dots distributed throughout each layer. These may be due to substrate roughness and the difference in Pt and Al₂O₃ step heights.

The 50 Å film shown in the topograph of Fig. 3(c) is relatively free of the pin holes observed at 30 Å. This film also appears to have a more pyramidal structure than the 30 Å film which may be due to a slightly higher deposition temperature of 590°C.

In conclusion, we have confirmed that in-air annealing of Al₂O₃(0001) produces atomically flat surfaces but sputter cleaning produces a long range surface corrugation that cannot be annealed out at a suitable temperature. We have also found that the character of epitaxial Pt films is very sensitive to deposition temperature and that continuous Pt films can be made for thicknesses between 30-50 Å. Two features of the 30 Å and 50 Å Pt films are evident: 1) although continuous and epitaxial, they are not ideal atomically flat surfaces; and 2) the substrate corrugation produced by sputtering plays a negligible role in preventing the formation of the ideal Pt film. However, it is not clear that such an ideal film is required for all applications and for magnetic multilayers and spin valves in particular. The question of whether these films are sufficiently smooth can only be answered through extending this study to subsequent depositions of magnetic structures.

This work was supported in part by the Office of Naval Research (N00014-89-C-0099)

References

- [1] S. S. P. Parkin, R. F. C. Farrow, R. F. Marks, A. Cebollada, G. R. Harp, and R. J. Savoy, *Phys. Rev. Lett.* **72** (1994) 3718.
- [2] R. F. C. Farrow, R. F. Marks, G. R. Harp, D. Weller, T. A. Rabedeau, and M. F. Toney, *Materials Science and Engineering R: Reports* **R11** (1993) 155.
- [3] D. E. Heim, R. E. Fontana Jr., C. Tsang, V. S. Speriosu, B. A. Gurney, and M. L. Williams, *IEEE Trans. Mag.* **30** (1994) 316.
- [4] J. M. Daughton, *Thin Solid Films* **216** (1992) 162.
- [5] R. F. C. Farrow, G. R. Harp, R. F. Marks, T. A. Rabedeau, M. F. Toney, and D. Weller, *J. Cryst. Growth* **133** (1993) 47.
- [6] the epitaxy of thick ($> 3000 \text{ \AA}$) magnetron sputtered Pt films has been studied with X-ray diffraction and transmission electron microscopy: B. M. Lairson, M. R. Visokay, R. Sinclair, S. Hagstrom, and B. M. Clemens, *Appl. Phys. Lett.* **61** (1992) 1390.
- [7] M. Yoshimoto, T. Maeda, T. Ohnishi, H. Koinuma, O. Ishiyama, M. Shinohara, M. Kubo, R. Miura, and A. Miyamoto, *Appl. Phys. Lett.* **67** (1995) 2615.
- [8] Y. Kim, and T. Hsu, *Surf. Sci.* **258** (1991) 131.
- [9] S. Chiang, R. J. Wilson, C. Gerber, and V. M. Hallmark, *J. Vac. Sci. Technol. A* **6** (1988) 386.
- [10] M. Gautier, J. P. Duraud, L. Pham Van, and M. J. Guittet, *Surf. Sci.* **250** (1991) 71.
- [11] T. M. French, and G. A. Somojai, *J. Phys. Chem.* **74** (1970) 2489.
- [12] J. Guo, H. L. M. Chang, and D. J. Lam, *Appl. Phys. Lett.* **61** (1992) 3116.

Figure Captions

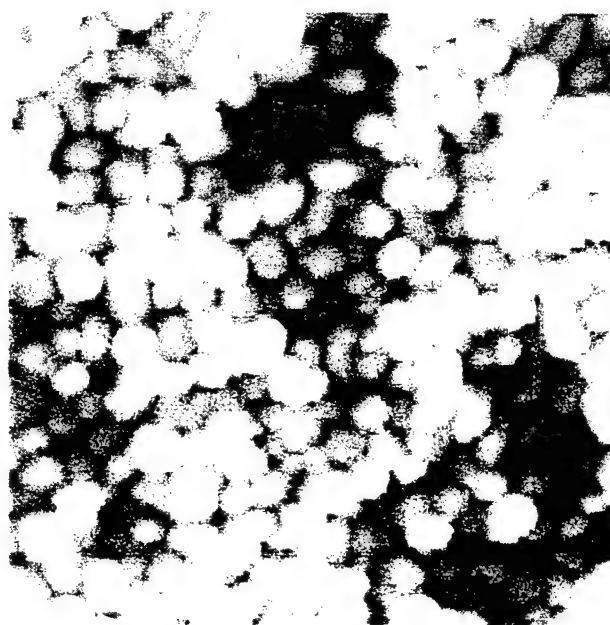
Fig. 1 STM images of 5 Å Pt films deposited at room temperature. (a) (2000 Å x 2000 Å) and (b) (600 Å x 600 Å) images for unsputtered Al₂O₃ substrate. (c) (2000 Å x 2000 Å) and (d) (600 Å x 600 Å) images for sputtered substrate.

Fig. 2 STM images of Pt films deposited at 580-590°C. 10 Å film: (a) (2000 Å x 2000 Å) and (b) (600 Å x 600 Å). 15 Å film: (c) (2000 Å x 2000 Å), (d) (600 Å x 600 Å), (e) (200 Å x 200 Å). 30 Å film.

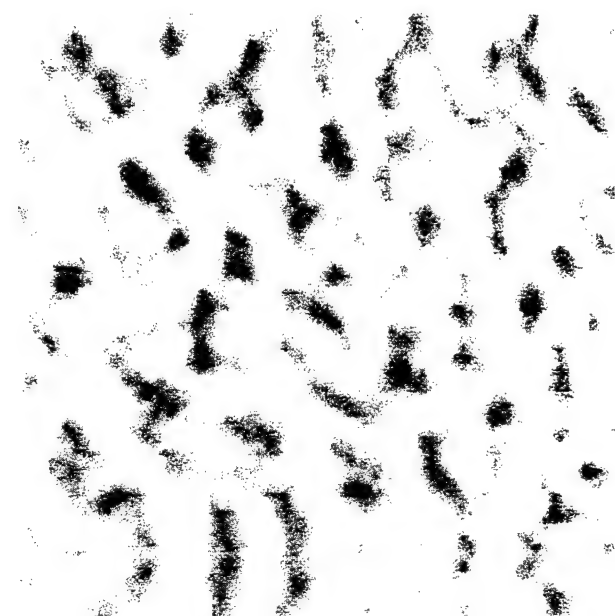
Fig. 3 STM images of Pt films deposited at 580-590°C. 30 Å film: (a) (2000 Å x 2000 Å) and (b) (600 Å x 600 Å) 50 Å film: (h) (2000 Å x 2000 Å).



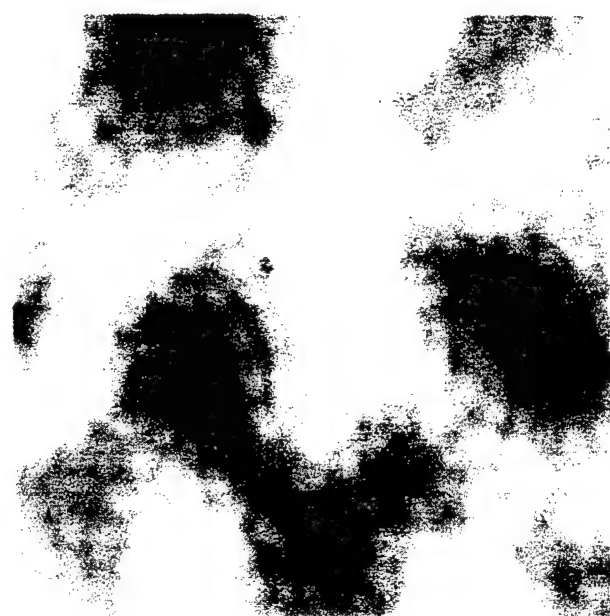
a



b



c



d

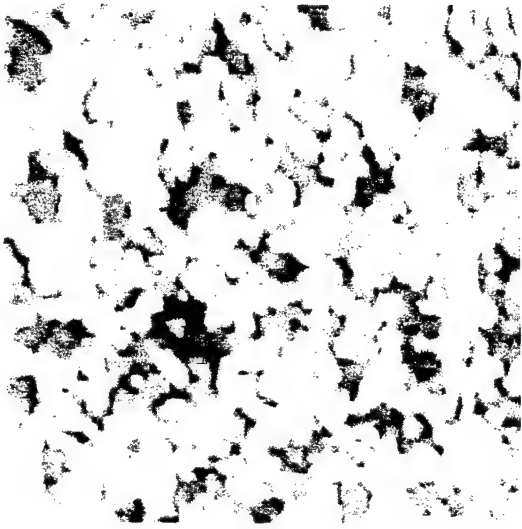
Fig. 1



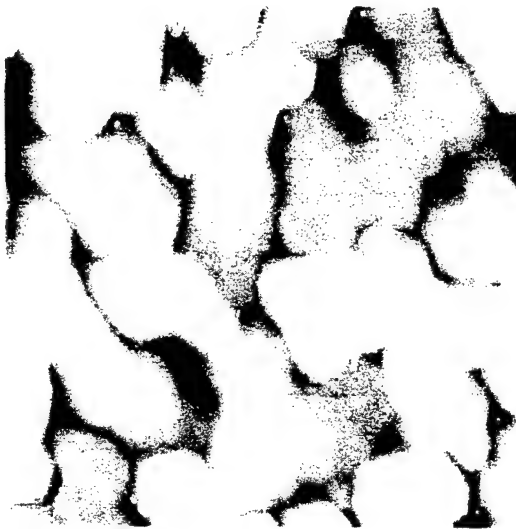
a



b



c



d



e

FIG 2



a



b



c

THE ROLE OF STRESS IN THE HETEROEPITAXY OF Au ON W(110)

M.L. Hildner, K.E. Johnson, and R. J. Wilson

IBM Research Division, Almaden Research Center, 650 Harry Road, San Jose CA
95120-6099

Abstract

The role of stress in forming a variety of Au film structures on W(110) is examined with scanning tunneling microscopy. The structural manifestations are different from those previously observed with STM because this system involves both an interface with mixed (tensile and compressive) strain and the Au(111) surface which reconstructs through strain relaxation. While sub-monolayer films already show isotropic strain relaxation through a combination of three uniaxial expanded structures, the complete monolayer is pseudomorphic. Strain relaxation then leads to a 2D dislocation structure in the second layer and a non-bulklike yet fully strain relaxed third layer. Stress is reintroduced for subsequent layers; this leads to the growth of flat-topped 3D crystallites, none of which are terminated by the fourth layer, and to the eventual formation of the uniaxially compressed surface reconstruction of Au(111).

The structures of surfaces and of epitaxially grown films are often dictated by the presence of stress. For single-crystal surfaces, stress is caused by the loss in coordination of atoms at the solid-vacuum interface and, if energetically favorable, can be relieved by atomic rearrangement [1]. In heteroepitaxy, the stress arises from the lattice mismatch between the substrate and film. Here, the film structure is determined by a subtle balance between E_ϵ , the energy of the elastic strain associated with a pseudomorphic film, and E_r , the interface energy associated with a relaxed, non-pseudomorphic interface [2,3]. In metal-on-metal systems with small lattice mismatch, E_ϵ of initial layers is often sufficiently smaller than E_r for the film to be pseudomorphic or commensurate. As the film thickens, E_ϵ increases and, after reaching a critical film thickness, the stress can be relieved by the formation of a weakly incommensurate phase consisting of misfit dislocations separating larger areas which are nearly commensurate. If E_ϵ becomes much larger than E_r , an incommensurate relaxed film can result.

For surfaces, the quintessential example of a stress relieved reconstruction occurs on the (111) surface of gold [1,4]. The reconstructed $(22 \times \sqrt{3})$ unit cell consists of two dense domain walls that separate larger areas that alternate between fcc and hcp stacking. The 4% compression is, on a local scale, unidirectional (along $[0\bar{1}1]$) and with fcc sites more energetically favorable than hcp sites, a paired stripe arrangement along $[\bar{2}11]$ arises. The relaxation is made more isotropic over long length scales — the domain walls bend by $\pm 120^\circ$ and form the so-called herringbone structure [5]. For epitaxial films, recent scanning tunneling microscopy (STM) studies have revealed a sequence of film structures resulting from the relaxation of tensile strain at metal-on-metal hexagonal interfaces. Cu films on Ru(0001) were observed to evolve from an initial pseudomorphically strained first layer to a fully relaxed bulklike Cu layer through a series of layers in which the strain is relieved either unidirectionally or more isotropically through the formation of high density misfit dislocations [3]. Similar structural manifestations for films relaxing from compressive stress have also been observed with STM but with low density misfit dislocations [3,6].

Stress also plays a role in determining the epitaxial growth mode. In the thermodynamic limit, the mode is determined by the interrelationship of the surface free energies of the substrate and n -layer film, γ_s and $\gamma_{f,n}$, respectively, and the interfacial energy, $\gamma_{i,n}$, which contains the thickness dependent strain energy of the film. Layer-by-layer or Frank-Van der Merwe (FM) growth is expected if $\gamma_s \geq \gamma_{f,n} + \gamma_{i,n}$. In heteroepitaxial systems, the strain energy increases with n so that the FM condition will no longer be valid at a critical film thickness, n^* , and 3D crystals form [Stranski-

Krastanov (SK) mode]. The Volmer-Weber (VM) mode, where 3D growth begins immediately, corresponds to $n^* = 1$.

In this paper, we describe the structural manifestations observed by STM in epitaxial Au/W(110) that arise from the relaxation of the mixed (tensile and compressive) strain at this fcc(111)/bcc(110) interface. A fully strained pseudomorphic Au lattice — with $\text{Au}[0\bar{1}1] \parallel \text{W}[001]$ — would have a negative misfit of -8.7% along $\text{W}[001]$ and a positive misfit of 11.8% along the perpendicular $\text{W}[\bar{1}10]$ direction in addition to the positive misfit of 5.4% along both $\text{W}[1\bar{1}1]$ and $\text{W}[\bar{1}\bar{1}1]$. Therefore, in reference to the W lattice, compression along $[001]$ and expansions along $[\bar{1}10]$, $[1\bar{1}1]$ and $[\bar{1}\bar{1}1]$ are expected and indeed observed as the Au film relaxes with increasing thickness. This mixture of expansion and compression leads to previously unobserved weakly incommensurate phases in the first two layers. Three layer films are essentially fully relaxed yet non-bulklike, but the accompanying transition of the underlying second layer occurs as a function of layer three coverage. The SK growth mode is observed with a critical thickness of four yet the flat topped crystallites that form never show a fourth layer top. As strain relaxation proceeds in thicker crystallites, surface dislocations emerge and evolve into the uniaxial compression structures of the Au(111) surface.

The STM and ultrahigh-vacuum system have been described elsewhere [7]. The Au films were evaporated from an alumina-coated W basket at a rate of ... determined by ... Films deposited at room temperature (RT) were rough showing kinetically limited three-dimensional growth. On the other hand, as the STM images will show, films that were subsequently annealed to 500°C showed characteristics of thermodynamic growth. This indicates that the structures observed under these conditions are energetically favored and driven by strain relaxation. The images were obtained at RT in the constant current mode at 0.1-1.5 V positive or negative tip bias and tunnel currents of 0.5-2.0 nA.

For Au films of less than 1 monolayer (ML), the surface is marked by numerous holes scattered about on partially filled terraces as shown in Fig. 1(a). There is also a subtle texturing in the form of bright ridges perpendicular to $[1\bar{1}1]$ and $[\bar{1}\bar{1}1]$ and shallow troughs along $[001]$. These features are only 0.2 Å high, occur at distances around 20 Å, and are frequently interrupted by the interspersed holes. As the coverage is increased to 1.5 ML, the holes fill in to result in smooth regions of layer one (L1) growth which are broken up by the same ridges and troughs as at lower coverage, but now spaced by hundreds of Å [Fig. 1(b) and (c)]. The patches between these stripe structures at both coverages show only atomic corrugation with spacings close to or identical to those of the substrate [Fig. 1(d)] implying that the Au is locally conformal to the W(110) surface. Fig. 1(d), an atomic resolution image of L1 in the vicinity of a ridge, also shows that as

the atomic rows cross the bright ridge they shift by less than the inter-row spacing. This implies that the registry of the Au lattice changes across the ridges. To explain this change in registry, we suggest that the Au atoms shift from the hourglass binding site of bcc materials towards the threefold hollow sites preferred by fcc materials of which there are two in the vicinity of each bcc site [these two sites are hereafter called left-handed (LH) and right-handed (RH) 3-fold sites]. The stripes are then readily attributed to misfit dislocations (domain walls) that separate the two types of domains expected.

With this interpretation it is apparent that strain relief appears in the first atomic layer of Au on W(110) and that it decreases with coverage. Fig. 2 shows a schematic of the L1 misfit dislocation structure. The bright ridges are low density walls that facilitate, on a local scale, a uniaxial expansion. The alignment of this expansion alternates between the $[1\bar{1}1]$ and $[\bar{1}11]$ directions. This alternation is reminiscent of the Au(111) herringbone structure and in similar fashion facilitates a more isotropic strain reduction. However, unlike Au(111), there is no pairing of lines since the LH and RH 3-fold sites are energetically equivalent. The increased height for the Au atoms in these walls is explained by their shift towards bridge sites. The dark troughs are also low density walls and create a uniaxial expansion in the $[\bar{1}10]$ direction. The fact that these walls are imaged as depressions must be explained by a reduced electron density (created by the expansion) as they contain no Au atoms at or near bridge sites.

For drawing simplicity, the domain walls in the model of Fig. 2 are narrower than those seen in the STM images [see Fig. 1(d)]. If the thickness of the ridges is increased beyond the six atoms of the model, the bond geometry within these walls changes. The preferred geometry of fcc Au(111) — hexagonal with 60° bond angles — is obtained at a ridge thickness of nine atoms. This appears to be the thickness observed in Fig. 1(d).

While not explicit, this structure does have some compression along $[001]$ which is imposed by the ridges. As demonstrated in Fig. 2, an examination along $[001]$ reveals that the distance spanned by a given number of atoms across the ridges is shorter than the distance for the same number of atoms outside the ridges (it is also observed that the ridges provide expansion along $[\bar{1}10]$). Regardless, there is clearly a stronger tendency toward relaxation of the compressive strain — including that resulting from the comparatively small misfit along the $[1\bar{1}1]$ and $[\bar{1}11]$ directions — as opposed to the tensile strain in this first layer. This is in accord with previous evidence from studies of isotropically strained interfaces that systems of positive misfit display dislocation structures in earlier layers than those of comparable negative misfit [8]. This phenomenon has been ascribed to the effectiveness of the steeply increasing repulsive

Morse potential in preventing film compression [3]. Apparently, this effectiveness is marginal for Au on W(110) since the film becomes (nearly) pseudomorphic at 1 ML.

An additional feature in the sub-monolayer films is the presence of voids at the junctions of the ridges. These are not depicted in the model, but are probably a consequence of a two-dimensional edge dislocation in the Au lattice formed at these unions. This dislocation creates an extra atomic row (seen along either $[\bar{1}11]$ or $[1\bar{1}1]$) inside the triangular shaped LH domain. In order to accommodate the extra row, the bond geometry inside the junction region must deviate more strongly than elsewhere in the film from the preferred hexagonal one; this makes such sites energetically unfavorable.

The observed structure conflicts with previous structural models [9,10] which were deduced from LEED patterns that we have verified in our measurements. These models predict a uniformly spaced atomic array with lattice spacings that match the W periodicity along W[001] and are slightly longer along W $[\bar{1}10]$; these would clearly give only 1D variations in the overlayer atomic positions. The LEED pattern, which shows superlattice beams spaced along $[\bar{1}10]$ and not along [001], arises instead from the superlattice of triangular domains being well correlated along $[\bar{1}10]$ but irregularly spaced along [001] as can be seen in Fig. 1(a).

As seen in Fig. 1(b), layer two (L2) is more highly corrugated, commences at the initial positions of the underlying substrate steps, which are clearly marked by rows of pinholes, and extends to smooth growth fronts of the step flow type. The atomic resolution image of Fig. 3(a) shows that L2 forms large perfect single domains which extend for hundreds of Å. The continuous bright ridges in these domains exhibit a "square wave" pattern that runs roughly along the [001] direction. There are also short vacancy rows, in periodic arrangement, that occur wherever neighboring square waves approach contact.

The precision of the periodic structures implies that L2 forms a weakly incommensurate phase that is locked into registry with the substrate on a length scale of tens of atoms. The ridges in the square wave pattern can then be ascribed to misfit dislocation structures separating regions where the second layer Au is nearly conformal to the underlying pseudomorphic first layer. It is tempting to model the transverse and longitudinal ridge segments as uniaxial compressions and uniaxial expansions, respectively, as this would provide for a packing that is closer along [001] and expanded in the perpendicular $[\bar{1}10]$ direction. However, such modeling leads to two-dimensional edge dislocations which are clearly not seen in the image of Fig. 3(a). Instead, this image shows nearly straight uninterrupted rows of Au atoms implying that both types of ridge

must include both compression along $[001]$ and expansion along $[\bar{1}10]$. This feature also implies that the L2 structure is nearly that of a strain relaxed Au net — *i.e.*, a Au net transformed from pseudomorphic by uniform compression along $[001]$ and uniform expansion along $[\bar{1}10]$.

Fig. 4(a) shows that by overlaying such a Au net on a W(110) lattice one can accurately map the L2 structure observed in the STM and determine how it deviates from the strain relaxed net. This mapping is generated by separating the second layer Au atoms into three groups: 1) those that lie within rectangular regions centered about the bcc binding sites (represented by open circles); 2) those that lie within rectangular regions centered about top sites (removed); and 3) the remainder (filled circles). This illustrates for the actual structure that the atoms of the first group are nearly conformal to the previous layer through a shift into sites that range approximately from the LH to the RH 3-fold sites, that the vacancy rows are due to a significantly smaller binding energy at top sites, and that the square wave domain walls are formed by atoms predominantly in bridge sites.

If L2 is formed by annealing deposits that slightly exceed 2 ML, Fig. 3(b), then a more heterogeneous L2 structure is formed in which the Au net shows some variability in alignment. The square wave structures are again evident in this image, but they change directions and some disorder can be seen in the regions separating different alignments. This orientational variability is not surprising given that this layer is nearly fully relaxed. Although the lateral atomic positions in a fully relaxed layer would be determined primarily by intra-layer atomic interactions, there would still be small strains induced by inter-layer atomic interactions that could be minimized by rotating the layer [11]. Apparently, intra-layer interactions are already predominant in L2 and such a rotation appears favored at the L1-L2 interface. However, inter-layer interactions are still appreciable since L2 is only near a fully relaxed structure and there is still a tendency for orientational alignment with the underlying layer.

By superimposing on Fig. 3(a) a net that is close to the imaged structure, it becomes clear that the second layer in this region is rotated with respect to the underlying lattice. By counting atomic spacings between the various features, the size of the mapping net and the rotation angle were determined and the map of Fig. 4(b) generated. The result is a net that is rotated by about 2° and that is much closer to the fcc geometry than the bcc one. In comparison to the fcc Au net there is a 4% compression along the $\text{Au}[\bar{2}11]$ direction and a 1% expansion along the $\text{Au}[01\bar{1}]$ direction. This is in contrast to the pseudomorphic layer where both values are close to 10%.

At this same 2.2 ML coverage, layer 3 (L3) islands are found and usually nucleate on the lower terrace at step edges. Fig. 5(a) shows a small L3 island which extends across a step edge where the lower terrace shows an essentially unrotated "square wave" structure much like Fig. 4(a) while the upper L2 terrace is primarily of the heterogeneous type. Running throughout the top of this L3 island is a series of lines that are aligned along $[\bar{1}10]$ and have a periodicity consistent with the L2 square wave pattern. Superimposed on this line structure is an oblong domain structure that substantially breaks the mirror symmetry of the W(110) surface and can be seen in a second domain orientation on other island tops.

On top of larger L3 islands, as illustrated in Fig. 5(b), the film structure changes substantially to form a moiré pattern that is consistent with an incommensurate isotropically relaxed overlayer on a W(110) lattice. Such a moiré pattern would not appear unless L2 changed to either a pseudomorphic layer or a relaxed layer identical to L3. The latter is most likely since the exposed L2 showed considerable relaxation and the addition of L3 should induce further relaxation. The small L3 islands, on the other hand, appear to be comprised of an isotropically relaxed third layer on top of the partially relaxed second layer "square wave" structure: the observed superimposed oblong domain and periodic line structures are consistent with the moiré pattern formed by this model.

When the coverage is increased above 3 ML the surface is nearly completely covered with the large island L3 structure, but in rare regions where the substrate steps are closely spaced the small island L3 structure can also be found. The lower left portion of Fig. 5(c) shows such a short terrace. In the upper right portion of this figure the film exhibits moiré patterns that have two different orientations and that show some structural imperfections at the step edge due to structural transformations of underlying layers. Clearly, the third layer is rotated — and exhibits two energetically-equivalent rotational domains — as a consequence of the strain energy dependence on the relative orientation of the Au and W lattices [11,12].

The existence of the large and small island types of L3 structure is apparently a size effect that may be described as follows. When considering only surface and interfacial energies, the third layer reduces the influence of the underlying substrate sufficiently to fully relax L2; but there is an energy cost associated with any transition boundaries separating partially and fully relaxed regions of L2. This energy cost is sufficient to prevent full L2 relaxation at low L3 coverages. However, as more surface is covered with L3, the energy cost of maintaining the interface between the square-wave L2 and the relaxed L3 increases until it is greater than the energy cost of any structural discontinuities in L2 that would arise at the perimeter of the L3 film.

Three-dimensional growth is observed at coverages above 3 ML. The 3D islands that form nucleate at the step edges and are always an atomic step higher than the adjoining terrace so that the island tops correspond to at least layer five (L5). Fig. 6(a) shows a wide scan image at 3.6 ML which shows that many of these islands spill over adjacent steps while remaining flat topped so that a progression of layers may be observed in a single island. The junction of these islands to the step edge involves very sharp, oriented multiple height steps as illustrated in Fig. 6(b). While this image shows some exposed layer four (L4), the combined observations of the commencement of 3D growth at L4 and the near overall absence of an exposed fourth layer suggests that there is a peak in the surface free energy as a function of film layer thickness: the surface free energy of L4 is larger than that of either L3 or L5.

Fig. 6(c) shows the L5-L6 transition of the island in Fig. 6(b). The diagonal height discontinuity in this image corresponds to the difference between the step heights of the Au and W surfaces. An extended linear defect originates at this transition and continues to the island edge. It can also be seen that the lines of maximum height locations are not all continuous across the layer transition. This shows that the six layer film has a somewhat different structure than the five layer film.

In rare cases, presumably associated with nucleation coincidences, islands are found to extend over several steps as in Fig. 7(a). This image was recorded with high pass filtering to reduce saturation effects of the six atom high step at the upper island edge which corresponds to L9. Line defects are again seen to originate at the step crossings with the density and direction of these defects varying as the island thickens [Fig. 7(a) and (b)]. Also, structural differences between successive layers are again evidenced by discontinuities in the lines of maximum height locations [Fig. 7(c)].

A possible explanation for these observations is that the third layer, though fully strain relaxed, is not bulk-like and that as the film thickens, it becomes more bulk-like. As the film does this, the surface layer experiences an increasing stress as is known from the Au(111) reconstruction. So the surface layer begins to show dislocations. Initially these are few and far between but steadily increase in number. Since the film is changing in more than one direction the dislocations also show directional variability. By layer nine they appear almost uniaxial and roughly aligned along the $A[\bar{2}11]$ direction the direction of the Au(111) reconstruction lines.

When such a surface is subsequently coated with an additional 4 ML and annealed then these islands can further develop into very tall finger like structures as shown in Fig. 8(a). Fig. 8(b), a higher magnification image which has been processed to eliminate the 10 atom high edges, shows an L3 structure on the base and a paired stripe reconstruction

on the island tops which matches the structure expected for a uniaxial $(22 \times \sqrt{3})$ Au(111) surface. At this thickness, steps do occur on the Au(111) fingers and it is still easy to detect the small height changes associated with substrate steps.

This work has demonstrated that a variety of surface, interfacial and island growth structures arise in the formation of epitaxial films of gold on W(110). Atomic resolution STM results are highly instructive and suggest atomic models which differ markedly from previously accepted models based on LEED.

Unexpected island growth phenomena are also observed at elevated coverages. We expect that many subtle new phenomena will be revealed by such high resolution imaging techniques as other materials, film thicknesses, and deposition techniques are explored.

This work was supported in part by the Office of Naval Research (N00014-89-C-0099)

References

- [1] R. J. Needs, M. J. Godfrey, and M. Mansfield, *Surf. Sci.* **242** (1991) 215.
- [2] F. C. Frank, and J. H. van der Merwe, *Proc. R. Soc. London A* **198** (1949) 205.
- [3] C. Günther, J. Vrijmoeth, R. Q. Hwang, and R. J. Behm, *Phys. Rev. Lett.* **74** (1995) 754.
- [4] C. Wöll, S. Chiang, R. J. Wilson, and P. H. Lippel, *Phys. Rev. B* **39** (1989) 7988.
- [5] J. V. Barth, H. Brune, G. Ertl, and R. J. Behm, *Phys. Rev. B* **42** (1990) 9307.
- [6] H. Brune, H. Röder, C. Boragno, and K. Kern, *Phys. Rev. B* **49** (1994) 2997.
- [7] S. Chiang, R. J. Wilson, C. Gerber, and V. M. Hallmark, *J. Vac. Sci. Technol. A* **6** (1988) 386.
- [8] R. Q. Hwang, J. Schröder, C. Günther, and R. J. Behm, *Phys. Rev. Lett.* **67** (1991) 3279.
- [9] E. Bauer, H. Poppa, G. Todd, and P. R. Davis, *J. Appl. Phys.* **48** (1977) 3773.
- [10] P. D. Augustus, and J. P. Jones, *Surf. Sci.* **64** (1977) 713.
- [11] J. P. McTague, and A. D. Novaco, *Phys. Rev. B* **19** (1979) 5299.
- [12] E. Bauer, and J. H. van der Merwe, *Phys. Rev. B* **33** (1986) 3657.

Figure Captions

Fig. 1 STM images of layers 1 and 2. (a) A 600Å wide image of a submonolayer deposit. (b,c) 2000Å, 600Å wide images at about 1.5 ml. (d) A 90Å wide image near a domain wall in (c).

Fig. 2 Model of first layer. Ridges and troughs are domain walls that separate two types of 3-fold hollow sites (RH and LH). To simplify the illustration, both types of domain wall are depicted as narrower than observed in the STM images. The ridges are comprised of uniaxial expansions that alternate between alignments along $[1\bar{1}1]$ (top ridge) and $[\bar{1}11]$ (bottom ridge). The troughs are uniaxial expansions along $[\bar{1}10]$. The dotted lines show that the ridge also provides some compression along $[001]$ — the distance spanned by the same number of atoms is less across than outside a ridge. The gray lines illustrate the two-dimensional edge dislocation formed at the junction of two ridges.

Fig. 3 STM images of layer 2. (a) Atomic resolution image (x) at 1.6ML showing ridges with "square wave" pattern and periodically arranged vacancy rows. (b) (x) image at 2.2 ML showing variability in orientational alignment.

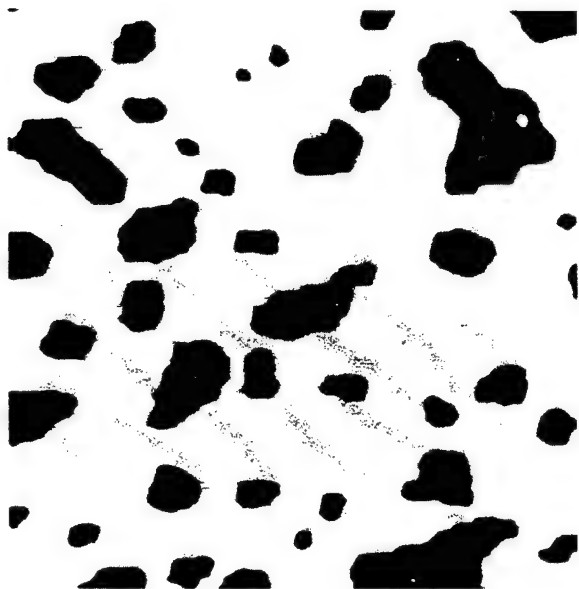
Fig. 4 Maps of the second layer structure generated by overlaying a relaxed Au net on a W(110) lattice (dark open circles). In the actual Au structure the conformal regions are formed by the shifting into hollow sites of atoms located near the bcc sites (gray open circles) and the "square-wave" structure is formed by atoms predominantly in bridge sites (solid circles). The vacancy rows occur where the Au would be in top sites. (a) and (b) are maps for 0° and 2° orientations of the net, respectively. The net, as determined from Fig. 3(a), is compressed by 4% along $Au[\bar{2}11]$ and expanded by 1% along $Au[01\bar{1}]$ in comparison to the fcc Au net.

Fig. 5 (600 Å x 600 Å) STM images of layer 3. (a) Small L3 topped island at 2.2ML that nucleated at step edge. The superposition of the oblong domain structure and the lines along $[\bar{1}10]$ — which have a periodic arrangement matching the L2 structures on the terraces — is consistent with a fully relaxed third layer on top of an unchanged second layer. (b) Large L3 topped island at 2.2ML where second layer has assumed fully relaxed L3 structure. (c) Terraces covered by three layers at 3.6ML. Upper right terrace has large island film structure in two possible orientations. Narrow terrace in lower left corner has small island film structure.

Fig. 6 STM images at 3.6ML show onset of three dimensional growth. (a) ($2\mu \times 2\mu$) image shows that islands nucleate at step edges and are flat topped. (b) () image showing typical junction of island at step edge. The island has a top that is an atomic step higher than the adjoining terrace and it spills over onto a second lower terrace. The top is therefore comprised of L5 and L6. (c) () image of L5-L6 transition of island seen in (b). The height discontinuity that extends from the lower right to the upper right is coincident with the underlying W step and is due to the difference in Au and W step heights. The linear defect originating at this layer transition is seen to extend to the island edge in image (b)

Fig. 7 STM images at 3.6ML showing island that extends over five terraces so that flat top goes from L5 to L9. For L6 to L9, line defects span layer transition boundaries. Their orientation changes and their number density increases with increasing thickness. Their alignment at L9 is roughly along $W[\bar{1}10]$ or $Au[\bar{2}11]$, the direction of the Au(111) reconstruction lines. (a) complete island (x), (b) L7-L9 (x), (c) L6-L7 (x).

Fig. 8 STM images of surface that has been annealed to 500°C after 4ML have been added to previously annealed 3.6ML covered surface. (a) (x) image shows very tall finger like island on 3ML covered terraces. (b) (x) image on top of island. Au steps now appear on island top. There are two small height discontinuities associated with the W substrate steps running from middle right to upper left. The paired strips of a Au(111) reconstruction are evident. (c) (x) image on top of island gives high magnification view of reconstruction strips.



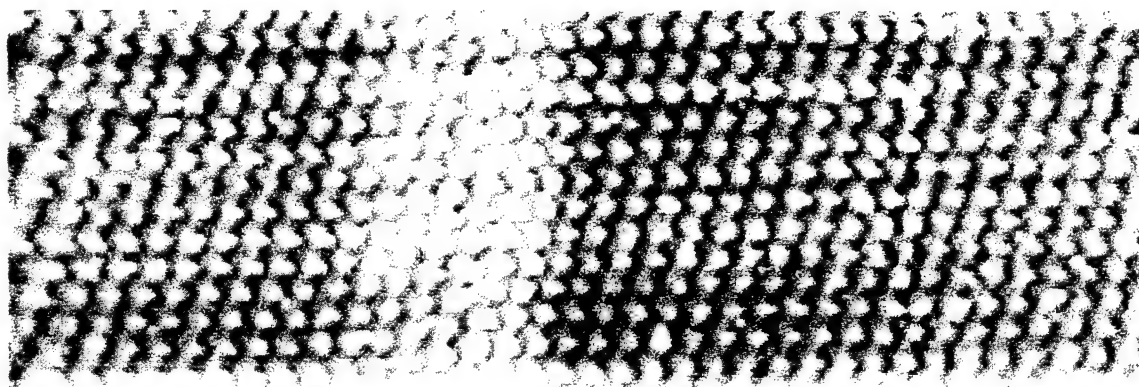
a



b



c



d

Fig 1

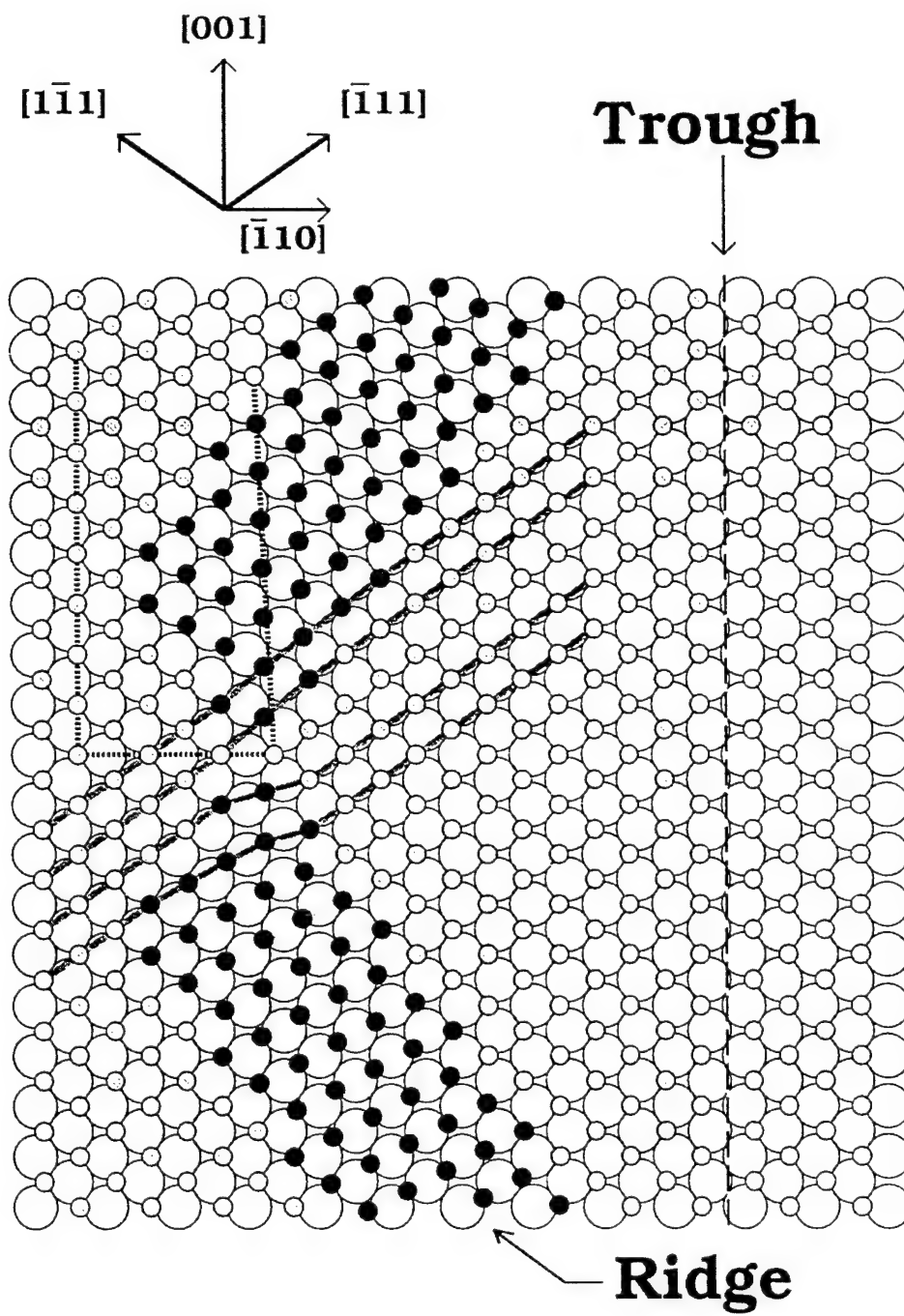
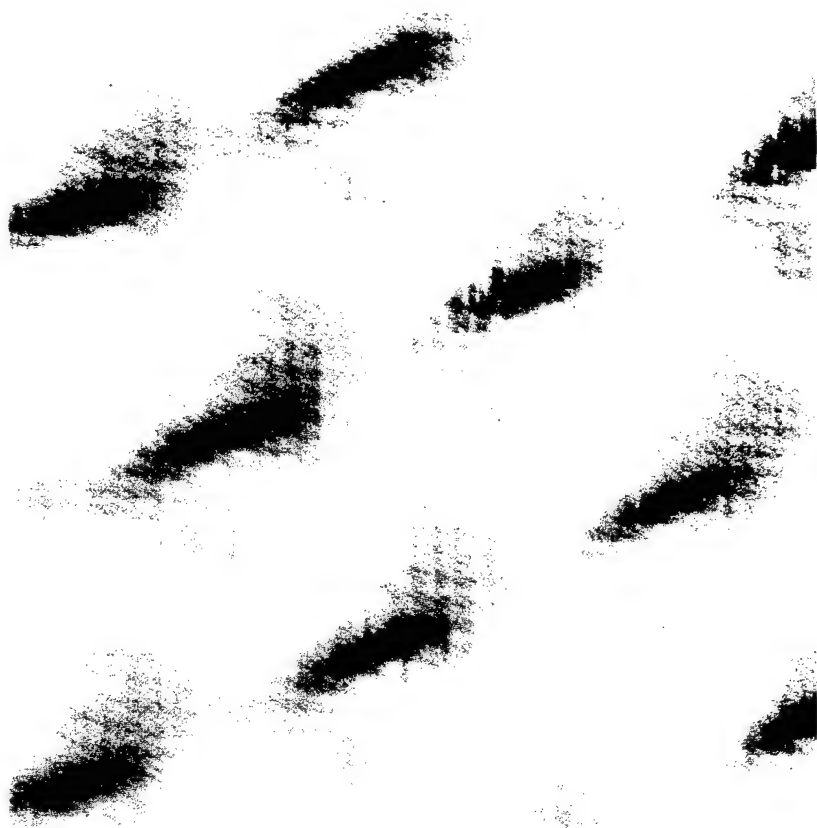
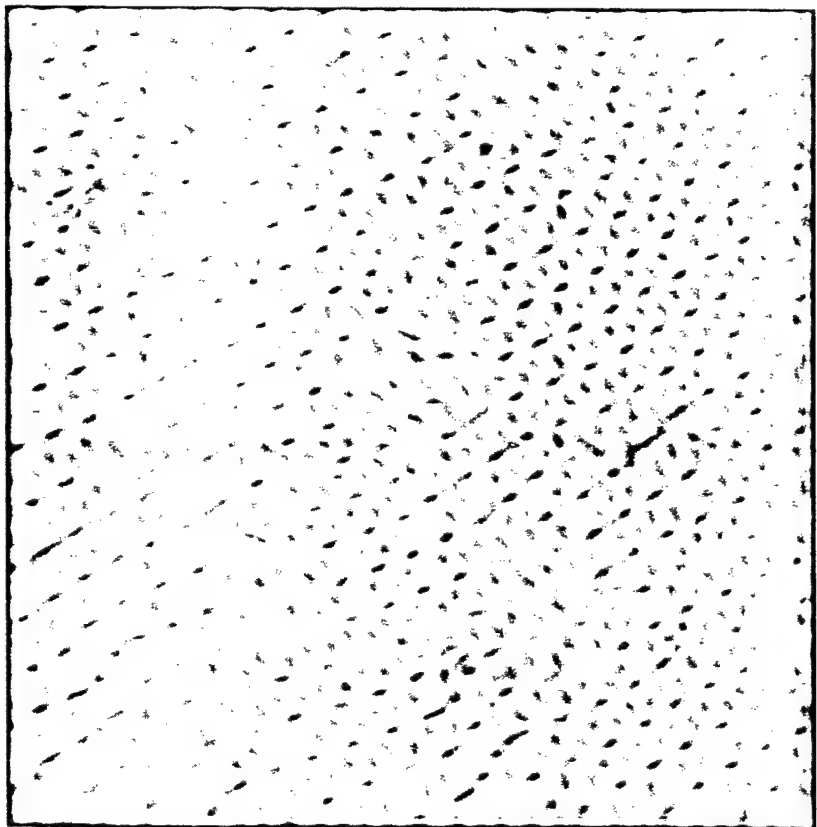


Figure 2

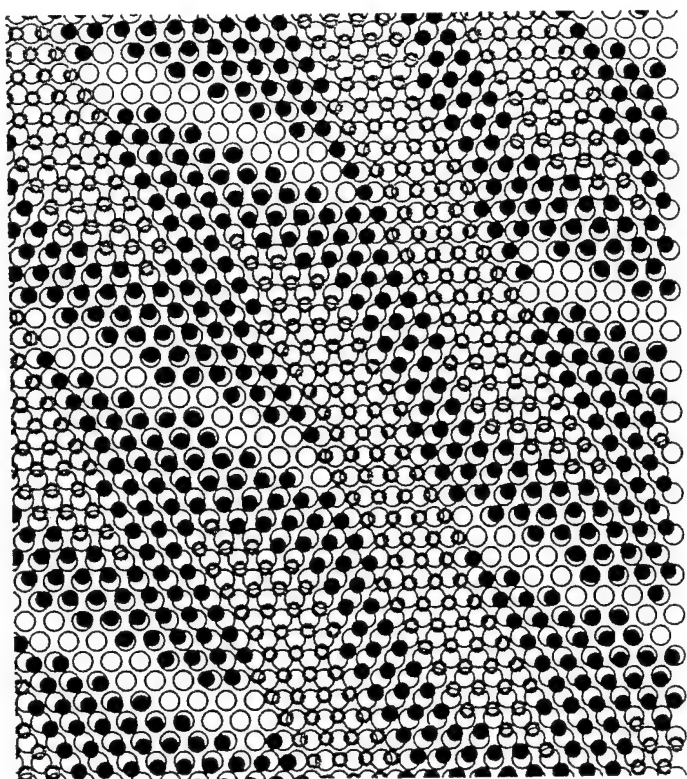


a

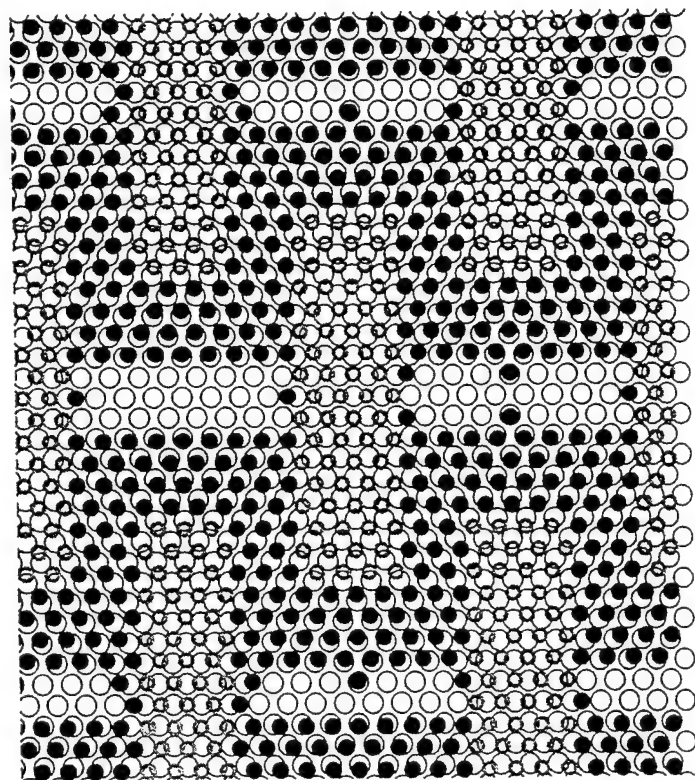


b

Fig 3



(b)



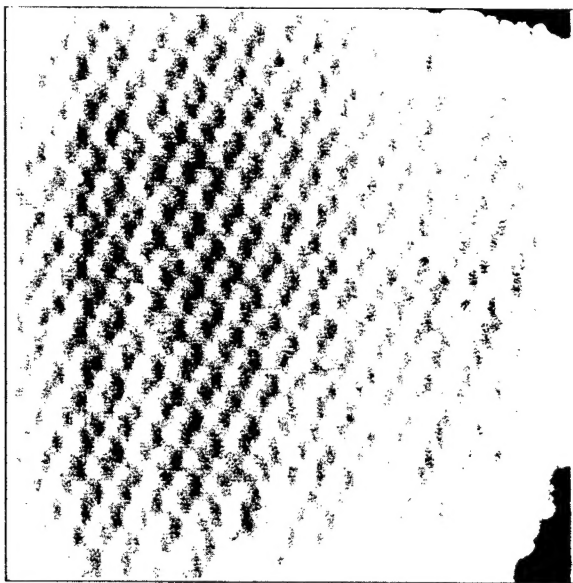
(a)

Figure 4

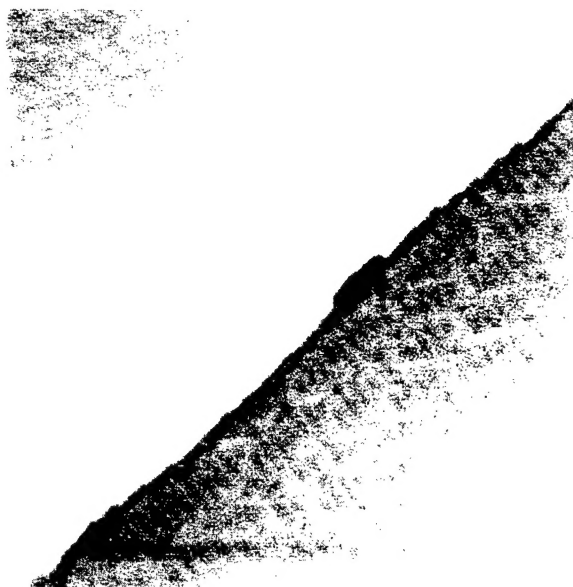
F104



a

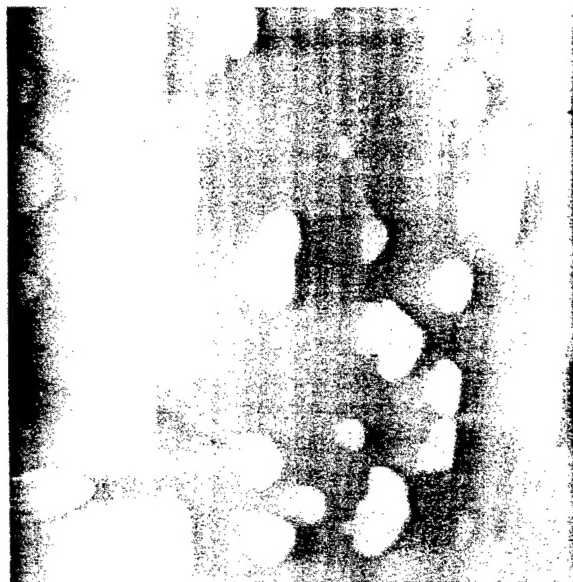


b

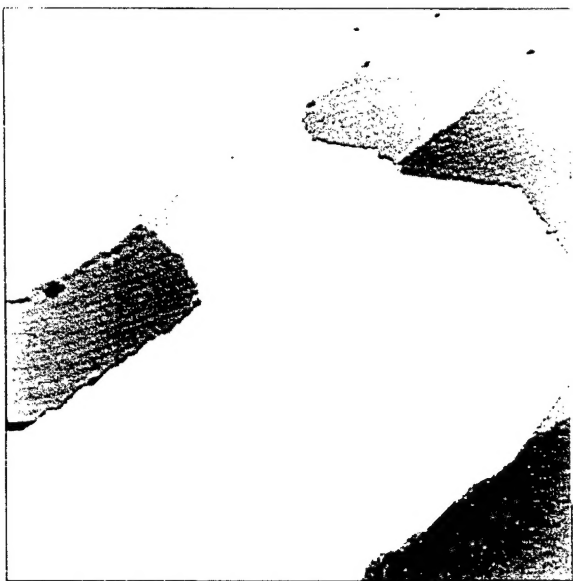


c

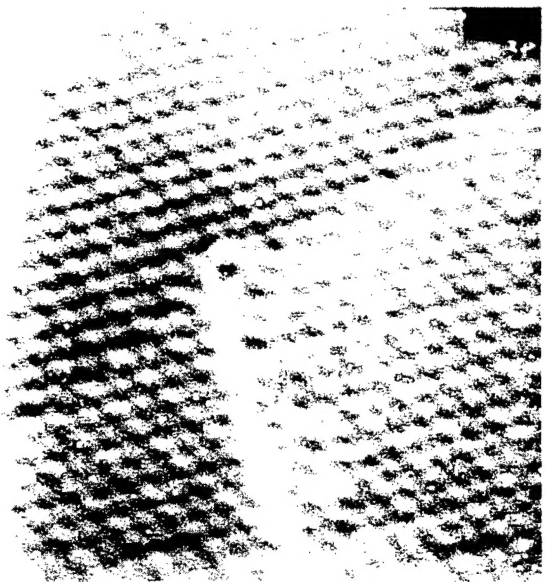
Fig 106



a

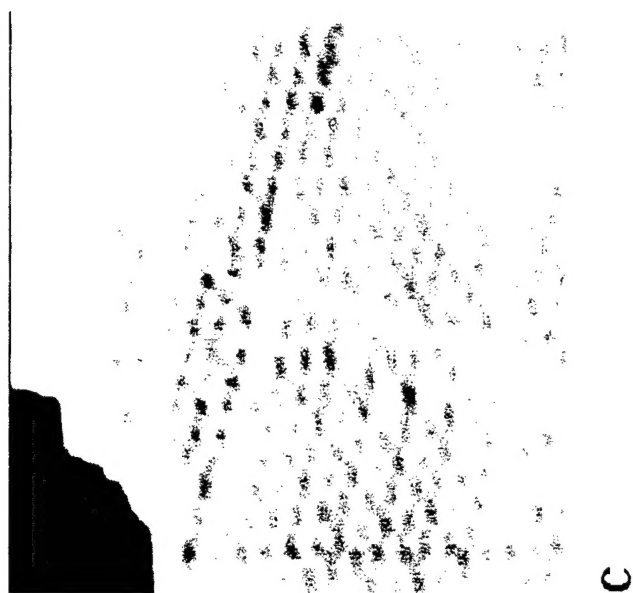
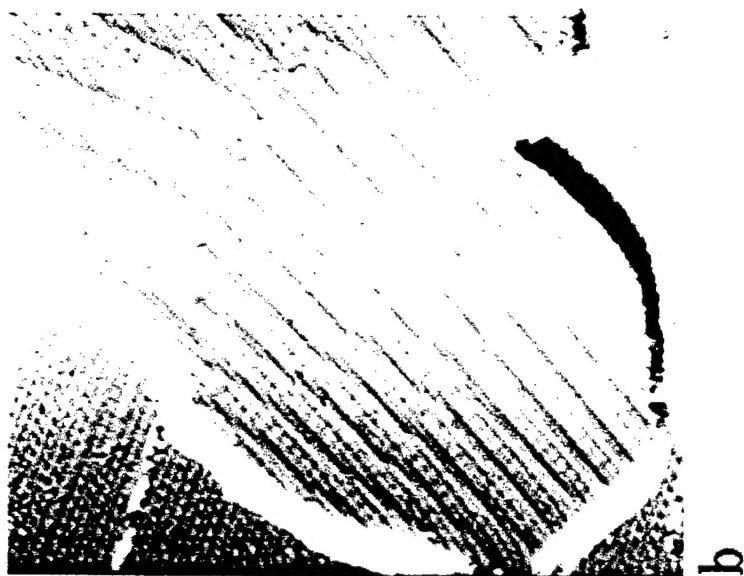


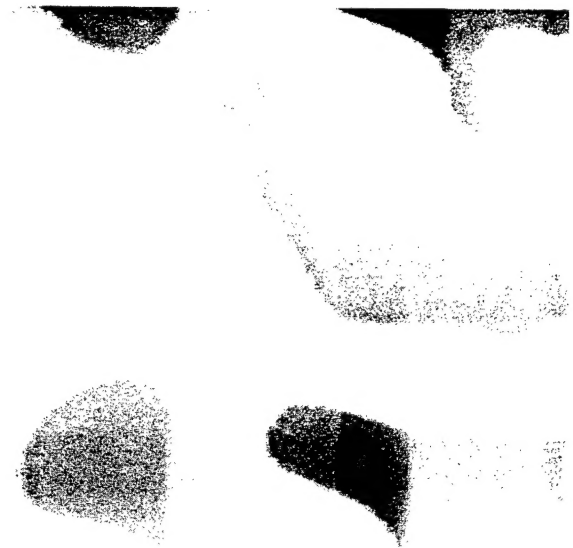
b



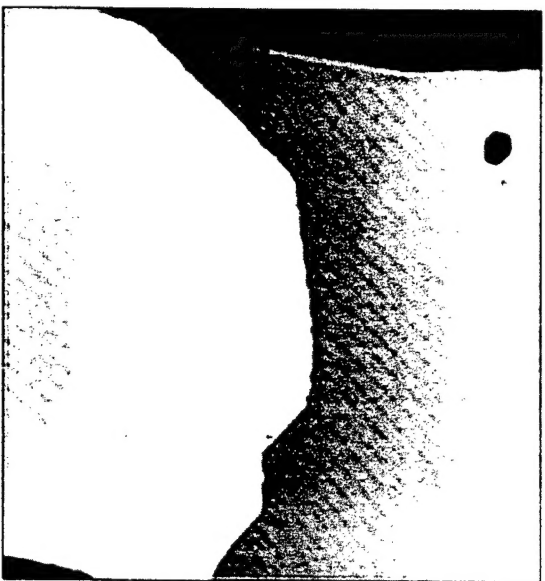
c

Fig 7





a



b



c